ISSN 2616-5775 Vol. 9, Issue 5: 9-19, DOI: 10.25236/AJCIS.2026.090502

Early Screening of Cesarean Scar Pregnancy Based on SHDSY-Net

Leqian Zheng[1,a], Jie Ying[1,b,*]

[1]School of Optical-Electrical and Computer Engineering, University of Shanghai for Science and Technology, Shanghai 200093, China
[a]372527834@qq.com, [b]yingjsh@163.com
**Corresponding author*

Abstract: *Cesarean scar pregnancy (CSP) is a rare form of ectopic pregnancy in which the gestational sac is implanted into the scar tissue of a previous cesarean section. It is a long-term complication of cesarean delivery, and its incidence continues to rise alongside the increasing cesarean section rate. To address the limitations of existing research in predicting severe hemorrhage using MRI features, as well as the scarcity of annotated data in pregnancy tissue testing and the reliance on experience for manual diagnosis, this paper proposes a multi-task deep learning model, SHDSY-Net, based on semi-supervised learning for early screening and risk assessment of massive bleeding in CSP patients. This model uses YOLOv8 as the backbone network and introduces the Mean Teacher semi-supervised learning framework. Through the teacher-student network structure and multi-scale pseudo-label enhancement module, it fully utilizes unlabeled data to improve the model's generalization ability. Experimental results show that, on the self-built pregnancy tissue (PT) dataset, the Dice coefficient reached 92.63% and the detection accuracy reached 92.31%. Meanwhile, the model can effectively predict the risk of intraoperative severe hemorrhage, providing an objective basis for clinical decision-making.*

Keywords: *Semi-supervised Learning, Pregnancy Tissue, SHDSY-Net, Cesarean scar pregnancy*

1. Introduction

Cesarean scar pregnancy (CSP) is a special ectopic pregnancy in which the pregnancy tissue is implanted into the previous cesarean scar tissue. It is a long-term complication of cesarean section [1]. Its incidence rate continues to rise with the rise of cesarean section rate, and the risk of occurrence increases significantly when the interval between two pregnancies is less than two years. Patients often have no obvious symptoms in the early stages, with some presenting as vaginal bleeding or abdominal pain [2]. Ultrasound features show that the implantation of pregnancy tissue into the scar area of the anterior wall of the lower segment of the uterus leads to emptiness of the uterine cavity and cervical canal, often accompanied by a high risk of bleeding [3]. Pregnancy products mainly include the gestational sac and its surrounding decidual tissue. Due to the risk of serious complications such as massive bleeding, shock, uterine rupture, and even hysterectomy if not treated in a timely manner, termination of pregnancy has become the main treatment strategy [4]. Among them, dilation and curettage (D&C) has become the most commonly used surgical technique due to its simple operation, but blind implementation may lead to serious complications that endanger the patient's life. The risk of intraoperative complications varies among patients with different conditions, and most patients can achieve minimal bleeding and complete removal of pregnancy tissue through D&C. Therefore, in order to reduce the incidence of surgical complications, more and more gynecologists are paying attention to predicting bleeding before pregnancy termination to assist in treatment decision-making and doctor-patient communication. However, there is currently no consensus on the best treatment plan for this complex disease [5].

In recent years, the application of MRI in the evaluation of cesarean scar pregnancy (CSP) patients has become increasingly frequent. With its multi-directional, multi parameter imaging technology and higher soft tissue resolution, it is superior to ultrasound in the diagnosis of CSP and evaluation of cesarean scar [6]. The current application mainly focuses on disease diagnosis, and research on the predictive value of MRI for large bleeding during dilation and curettage (D&C) surgery is still limited. Previous studies have tended to evaluate the predictive power of a single specific MRI sign, but have

ISSN 2616-5775 Vol. 9, Issue 5: 9-19, DOI: 10.25236/AJCIS.2026.090502

not comprehensively analyzed the predictive ability of multiple MRI signs for large bleeding [7]. Therefore, this study aims to establish an early screening model for cesarean scar pregnancy based on SHDSY-Net to predict the risk of major bleeding in CSP patients before surgery.

Early detection and segmentation of pregnant tissue is crucial for assessing pregnancy risks and developing clinical intervention plans, especially for uterine scar areas with a history of cesarean section. Accurately locating the spatial relationship between pregnant tissue and uterine scars can help reduce the risk of complications and ensure maternal and infant safety [8]. However, manual diagnosis relies on the experience of doctors, which may lead to problems such as long-time consumption and low consistency in interpretation, which may result in missed or misdiagnosed cases. Therefore, automated detection technology for pregnancy tissue is particularly important. Through rapid identification and localization, it can reduce human errors and improve the efficiency of large-scale case screening [9]. MRI, with its high-resolution soft tissue imaging and multi plane reconstruction capabilities, can clearly display the anatomical relationship between pregnancy tissue and uterine wall, providing key imaging evidence for automated detection. Pelvic MRI can more accurately present the internal structure of the uterine cavity in early pregnancy, suitable for analyzing the position of pregnancy tissue and its adjacent relationship with the uterine muscle layer. The imaging manifestation is that the gestational sac is usually circular or elliptical, while the decidua tissue is distributed in patches [10].

Deep learning models, with their efficient feature learning capabilities, have significantly promoted the clinical translation of medical image detection and segmentation technology. In the field of medical image processing, deep learning technology has been widely applied in the segmentation and detection tasks of uterus and its lesions. Shahedi et al. [11] proposed a system based on Convolutional Neural Network (CNN) that can automatically extract MRI image features and achieve accurate segmentation, improving segmentation efficiency and measurement accuracy. Guo et al. [12] proposed an improved Swin-Unet network that combines wavelet convolution and attention mechanism for MRI segmentation in HIFU treatment of uterine fibroids. Singh et al. [13] proposed an ensemble method based on cellular neural networks, which not only accurately identifies tumor regions, but also calculates tumor volume more precisely through improved algorithms, and achieves rapid radiomics analysis for risk stratification. Cai et al. [14] proposed a lightweight hybrid model combining MobileNetV2 and deep convolutional generative adversarial networks for the recognition of uterine fibroids in ultrasound images, and improved the model's generalization ability and robustness by generating enhanced data; Yin et al. [15] proposed a high-precision system that utilizes an improved level set algorithm and convex polygon optimization technique to accurately segment the boundaries of the gestational sac in ultrasound images.

However, although these studies have achieved important results in the segmentation and detection of uterus and its lesions, there are still some limitations: manual assistance may be required to ensure accuracy in complex MRI image segmentation. In addition, currently available multimodal imaging datasets of pregnancy tissues are scarce, and related detection and segmentation research is mostly limited to a single target. Zong et al. [16] proposed a deep learning model based on multi sequence MRI images for evaluating the risk of adverse pregnancy outcomes in patients with placental implantation. El Hatib et al. [17] proposed a deep learning-based segmentation system that combines convolutional neural networks to identify and analyze key ultrasound image features, and uses data augmentation and multi-scale feature learning to improve segmentation performance. Li et al. [18] proposed a column chart prediction model based on multimodal ultrasound parameters, which integrates multiple ultrasound examination indicators such as two-dimensional, color Doppler, and three-dimensional to quantitatively predict the bleeding risk of CSP patients undergoing hysteroscopic curettage before surgery, achieving risk stratification management. The above research has made some progress in the field of pregnancy tissue imaging, but there are still limitations: the scarcity of publicly available multimodal imaging datasets has led to related studies being limited to a single target, making it difficult to fully cover the complexity of pregnancy tissue.

Unlike existing research, this paper proposes a medical image segmentation model SHDSY-Net. This model has multi task learning ability and can simultaneously handle detection and segmentation tasks. The model uses YOLOv8 as the backbone network, integrating efficient spatial feature extraction and multi-scale feature fusion mechanisms to enhance the understanding of spatial relationships in pregnant tissues and improve detection accuracy. By using channel attention and dimension matching modules to screen key features, and combining transposed convolution and bilinear interpolation to achieve cross scale feature fusion, the clarity of segmentation boundaries is optimized. In addition, a single head self-attention mechanism [19] is adopted to capture global contextual information, and multi

ISSN 2616-5775 Vol. 9, Issue 5: 9-19, DOI: 10.25236/AJCIS.2026.090502

task coupling of detection and segmentation tasks is achieved through residual connections and gradient propagation. Experiments conducted on the Pregnancy Tissue (PT) dataset and the open-source Automated Cardiac Diagnostic Challenge (ACDC) dataset have shown that the proposed method outperforms existing research methods in multiple evaluation metrics. Meanwhile, a quantitative scoring model based on MRI features (uterine scar thickness, gestational sac diameter, scar tissue area) can effectively predict the risk of major bleeding during D&C surgery, providing objective basis for clinical decision-making.

2. SHDSY-Net Model

2.1 SHDSY-Net Model Architecture

Given the scarcity of annotated data in current research on pregnancy tissue detection, semi supervised learning methods have become a research hotspot, as they can improve model generalization ability by combining a small amount of annotated data with a large amount of unlabeled data. This method can explore potential features in unlabeled data, helping the model better understand images of pregnant tissue in the uterus. The design of the semi supervised learning network in this article follows the Mean Teacher semi supervised learning method [20]. To address the challenges of pregnancy tissue detection and segmentation, this paper proposes a semi supervised network SHDSY-Net aimed at achieving both pregnancy tissue segmentation and detection tasks simultaneously. The overall framework of SHDSY-Net is shown in Figure 1. The dataset is divided into two parts: labeled data and unlabeled data, and different enhancement strategies are applied to both. For annotated data, only strong enhancement is used. When teacher networks generate pseudo labels using unlabeled data, weak enhancement is first applied [21]. During the process of student network training, both labeled and unlabeled data are used simultaneously, with the unlabeled data being subjected to strong enhancement processing. To ensure the quality of generating pseudo labels, this paper introduces a multi-scale pseudo label enhancement module in the pseudo label generation stage.

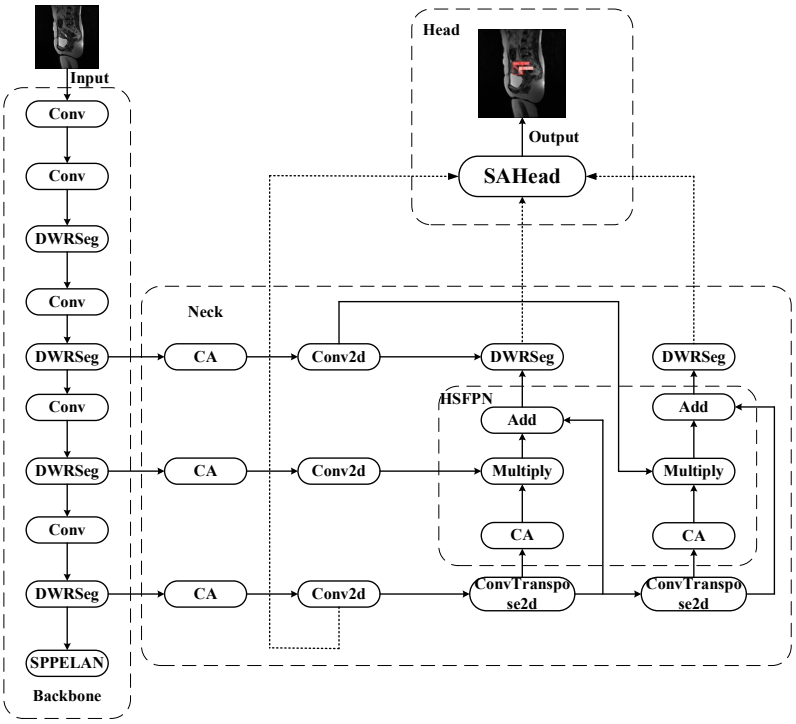

Figure 1: Network architecture of SHDSY-Net

To ensure that the generation of pseudo labels is not affected by network fluctuations, the teacher network parameters are updated using the exponential moving average of the student network parameters [22]. This technology can smooth the update process of teacher network parameters, making pseudo labels more stable, while reducing the uncertainty caused by drastic parameter fluctuations during training. This stability enhances the reliability of pseudo labels, thereby optimizing the overall performance of semi supervised learning frameworks.

ISSN 2616-5775 Vol. 9, Issue 5: 9-19, DOI: 10.25236/AJCIS.2026.090502

This article introduces a multi-scale pseudo label enhancement module in the pseudo label generation stage. This module aims to improve the quality and stability of pseudo label generation in semi supervised learning processes. Specifically, when predicting unlabeled data in teacher networks, weak enhancement is first applied to generate initial pseudo label boxes; Then, a multi-scale enhancement strategy is adopted to transform the same input image at different scales, generate multiple views, and perform object detection on each view to obtain corresponding prediction boxes. These multi-scale prediction boxes are fused and filtered through non maximum suppression to obtain consistent and robust pseudo labeled boxes. Ultimately, these pseudo labels are used to guide the training of student networks on strongly enhanced data.

In SHDSY-Net, the backbone is responsible for extracting features from input images, consisting of multiple convolutional layers (Conv), efficient spatial feature extraction modules, and context information capture modules. Backbone outputs a series of feature maps of different scales, which are passed to the neck network for further processing. Neck serves as a bridge connecting Backbone and the detection head, primarily responsible for fusing feature maps of different scales to enhance feature representation. Neck consists of multiple convolutional layers (Conv2d, ConvTranspose2d), an efficient spatial feature extraction module, and a multi-scale feature fusion module. The Head is responsible for the final object detection and segmentation tasks, consisting of a lightweight self-attention detection head SA Head module.

The proposed framework consists of four core modules: 1) Efficient spatial feature extraction: The SPPELAN module in the backbone network processes the input image through convolutional layers and activation functions to generate feature maps. Multi scale features are obtained through spatial pyramid pooling, and then fused into a unified feature map for subsequent tasks. 2) Multi scale feature extraction: The channel attention module and dimension matching module screen and unify the multi-scale feature map, and the selective feature fusion mechanism combines high-level and low-level features. 3) Context information capture: The region and semantic localization module extracts local deep semantic features, and generates multi-scale contextual feature maps for segmentation tasks through feature fusion, dilated convolution, and residual concatenation. 4) Lightweight self-attention: 1 × 1 convolution is used to reduce the number of feature map channels and computational complexity. Multi head self-attention layers enhance global context awareness, and then the channel dimension is restored through 1 × 1 convolution; The self-attention output is overlaid with residual connections and auxiliary gradient propagation onto the original feature map, and the final output is used for both detection and segmentation tasks.

2.2 Efficient spatial feature extraction and multi-scale feature fusion methods

The efficient spatial feature extraction module is one of the components of YOLOv9, which combines spatial pyramid pooling and efficient layer aggregation network to integrate multi-scale feature maps, enabling the model to better understand image contextual information and improve detection performance. This module optimizes feature flow through gradient path planning, reduces information loss in deep networks, and achieves lightweight and high-precision feature extraction [23].

The multi-scale feature fusion method used in the research institute consists of two main parts: the feature selection module and the feature fusion module.

The feature selection module uses channel attention module and dimension matching module to filter multi-scale feature maps and unify the number of channels.

$$f_{\text{in}} \in R^{C\times H\times W} \tag{1}$$

The channel attention module processes the input feature map, where C represents the number of channels, H represents the height, and W represents the width. Global average pooling and global maximum pooling generate channel weights through Sigmoid activation function.

$$f_{\text{CA}} \in R^{C\times 1\times 1} \tag{2}$$

The dimension matching module Caitong uses a 1x1 convolution to reduce the number of channels to 256. The feature fusion module, as the core component, fuses the extended high-level features with low-level features through a selective feature fusion mechanism, and adjusts the size through transpose convolution and bilinear interpolation to obtain an enhanced feature representation [24].

$$f_{\text{high}} \in R^{C\times H\times W} \tag{3}$$

ISSN 2616-5775 Vol. 9, Issue 5: 9-19, DOI: 10.25236/AJCIS.2026.090502

$$f_{\text{low}} \in R^{C\times H_1\times W_1} \tag{4}$$

$$f_{\widehat{\text{high}}} \in R^{C\times 2H\times 2W} \tag{5}$$

$$f_{\text{att}} \in R^{C\times H_1\times W_1} \tag{6}$$

$$f_{\text{out}} \in R^{C\times H_1\times W_1} \tag{7}$$

The process of feature selection fusion can be expressed as:

$$f_{\text{att}} = \text{BL}\left(T - \text{Conv}\left(f_{\text{high}}\right)\right) \tag{8}$$

$$f_{\text{out}} = f_{\text{low}} \times \text{CA}\left(f_{\text{high}}\right) + f_{\text{att}} \tag{9}$$

Among them, the combination of transposed convolution and bilinear interpolation is used to adjust the size of high-level feature maps. Bilinear interpolation achieves size adjustment in a computationally efficient manner, while transposed convolution not only upsamples feature maps, but also reconstructs input data through zero padding and convolution to solve non-uniform sampling problems.

This combination of transpose convolution and bilinear interpolation to adjust the size of advanced feature maps can better meet the needs of image sampling. Bilinear interpolation, with its simplicity and speed of calculation, effectively achieves the adjustment of image size. And transposed convolution not only enlarges the size of the feature map through its trainable parameters, but also reconstructs the input data in the form of convolution by zero padding after the feature map is expanded. In addition, transposed convolution can effectively solve the problem of non-uniform sampling by selectively sampling the input image at different positions in the output image. The schematic diagram of the feature fusion module is shown in Figure 2.

The lightweight self-attention detection head module aims to optimize the use of computing resources while maintaining effective capture of global contextual information [25]. Unlike research that directly applies traditional Transformer mechanisms, this paper adopts a more streamlined approach that only uses a single head self-attention layer to achieve global context awareness and improve computational efficiency.

The DWR Seg extended residual module extracts multi-scale contextual information through two steps: regional residual and semantic residual [26]. The core of DWR Seg is the DWR module, which first generates clear regional feature maps through standard convolution. Then, in the semantic reconstruction stage, depth separable convolution is applied to the generated regional feature maps. However, unlike traditional operations, only a single receptive field is used for morphological filtering.

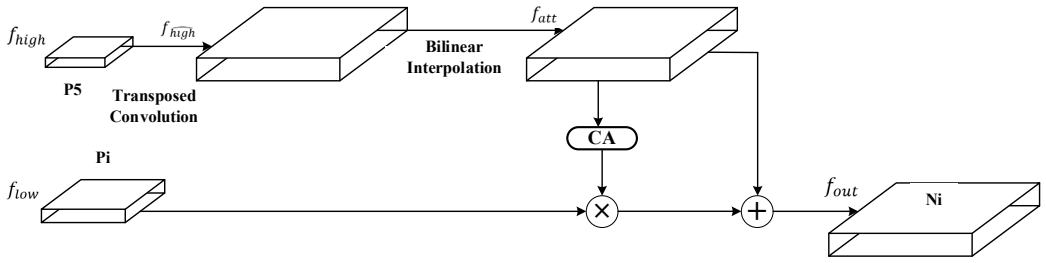

Figure 2: Select feature fusion module

2.3 Scoring method for predicting the degree of severe bleeding in cesarean scar pregnancy

Calculate the following MRI features: (1) Uterine scar thickness: Measure the thinnest scar thickness in the uterus on the MR image; (2) Cesarean section diverticulum (CSD) depth: Measure the vertical distance from the deepest point of the diverticulum to the entrance of the diverticulum on MR images; (3) Cesarean section diverticulum (CSD) area: Detect the diverticulum area formed by the invasion of the gestational sac into the uterine scar on MR images.

In the training queue, univariate and multivariate logistic regression analyses were used to identify the independence between MRI features and major bleeding. Each independent risk factor identified in the multiple factor analysis is assigned a score of 1, and a risk scoring model is constructed [26]. The

ISSN 2616-5775 Vol. 9, Issue 5: 9-19, DOI: 10.25236/AJCIS.2026.090502

optimal cut-off value for dividing patients into low-risk and high-risk groups was determined by calculating the characteristic curve (ROC) index. ROC was used to evaluate the effectiveness of the scoring model in predicting major bleeding during uterine curettage surgery, with area under the curve (AUC) values ranging from 0.5 to 1.0, where 0.5 represents random guess and 1.0 represents perfect match. In addition, the sensitivity, specificity, accuracy, positive predictive value, and negative predictive value of the scoring model were calculated separately. The predictive performance of this scoring model will be further validated in the validation queue. Three independent risk factors (uterine scar thickness, gestational sac diameter, and scar tissue area) determined through multiple logistic regression analysis were used to construct a scoring model. When each independent risk factor is positive, 1 point is assigned: 1 point for patients with uterine scar thickness ≤ 2.25mm, 1 point for cesarean section diverticulum (CSD) thickness ≥ 8.75mm, and 1 point for cesarean section diverticulum (CSD) area ≥ 163.50mm^2. Therefore, this study established a risk scoring model with a total score of 3, distinguishing between low-risk (total score<2) and high-risk (total score ≥ 2) through the optimal cutoff value of 2. The schematic diagram of the relationship between the gestational sac and the diverticulum in cesarean section is shown in Figure 3. Among them, a is the thickness of the scar, b is the depth of the diverticulum, c is the diameter of the gestational sac, and s is the area of the cesarean section diverticulum (CSD).

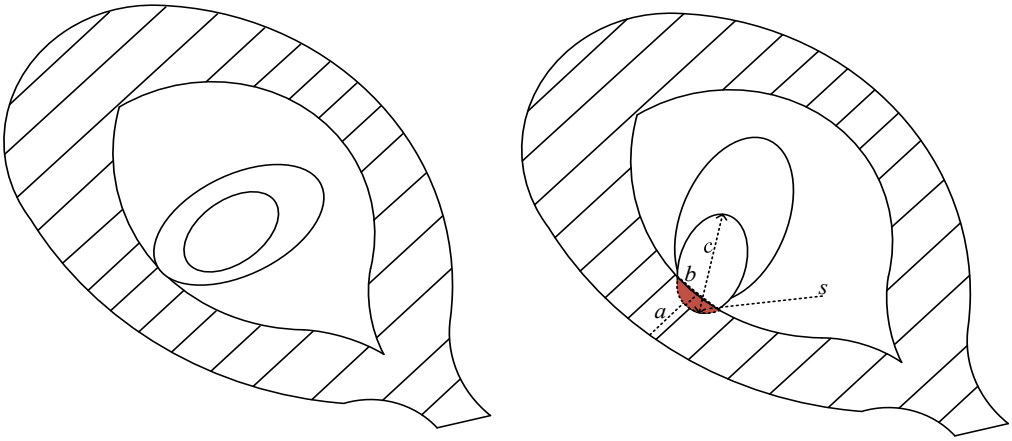

Figure 3: Illustration of the position relationship between gestational sac and CSD

3. Experimental environment and dataset construction

3.1 Data Preprocessing

In the data preprocessing stage, due to the strict requirements of YOLOv8 in terms of dataset, image labels require TXT standard format files, and image data images require image files. And the dataset we obtained is in NRRD format image files. We need to convert the original NRRD files into NII files through Python language processing, then convert the NII files into DCM files through Python language processing, and finally generate 2D image slices from the DCM files through DICOM software. The specific data preprocessing process is shown in Figure 4.

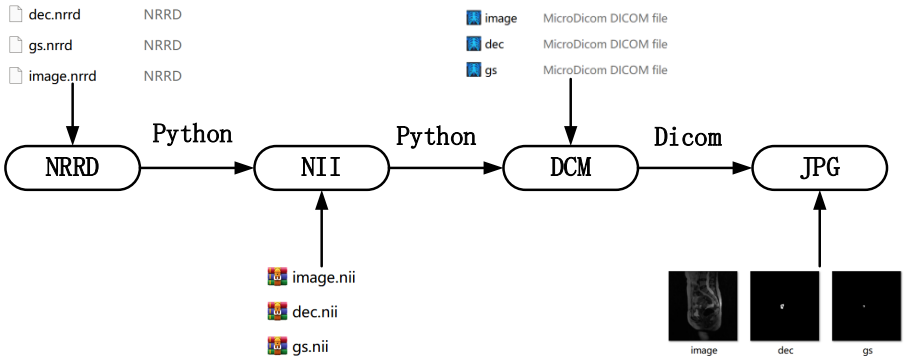

Figure 4: Schematic diagram of data preprocessing

ISSN 2616-5775 Vol. 9, Issue 5: 9-19, DOI: 10.25236/AJCIS.2026.090502

3.2 Dataset Construction and Parameter Setting

Validate the performance of our method by evaluating it on a self-made pregnancy tissue (PT) datasets and an open-source cardiac ACDC datasets. The PT datasets contains images of 82 patients who underwent MRI examinations at Shanghai First Maternity and Child Health Hospital. After screening and data preprocessing, a total of 400 two-dimensional MRI slices were obtained, all of which contained gestational sac (GS) and decidual tissue (DT). The MRI examination was performed using a 1.5T device (Optima MR360) and phased array coils. The acquisition parameters are as follows: repetition time/echo time [TR/TE] is 4000~5800/72~125ms; layer thickness is 4-5mm; matrix size is 320 × 192; Flip angle 150 °; Bandwidth 320Hz; image resolution 512 × 512. The open-source ACDC dataset contains 150 clinical cases of cardiac MRI, covering both normal and diseased hearts. This study utilized this dataset for multi task learning, including segmentation and detection of left ventricular LV, myocardial MY, and right ventricular RV. 400 two-dimensional image slices were selected and divided into training, validation, and testing sets in an 8:1:1 ratio. The annotation mask (Ground Truth) in the dataset is used as the evaluation criterion.

Model training activates computer nodes through command-line instructions to start. The training hyperparameter settings are shown in Table 1. All experiments were run on the Microsoft Windows 10 operating system, with the server configured as an AMD Ryzen 7 7840H central processing unit (integrated with Radeon 780M graphics card).

Table 1: Hyperparameter settings for model training

Image resolution	Training cycle	Learning rate	Batch size	Hsv_h
640*640	200	0.01	16	0.015
Hsv_s	Hsv_v	Filp_lr	Translate	Mosaic
0.7	0.4	0.5	0.1	1.0

The performance of SHDSY-Net multitask learning network is quantitatively evaluated using Dice similarity coefficient, Mean Intersection over Union (MIoU), Intersection over Union (IoU), Recall (R), Precision (P), F1 score, and Average Precision (AP) to measure the detection and segmentation performance on two datasets. The calculation methods for each indicator are as follows:

$$P=\frac{\mathrm{TP}}{\mathrm{TP+FP}} \tag{10}$$

$$R=\frac{\mathrm{TP}}{\mathrm{TP+FN}} \tag{11}$$

$$\mathrm{F1}=\frac{2\times P\times R}{P+R} \tag{12}$$

$$\mathrm{AP}=\frac{\mathrm{TP+TN}}{\mathrm{TP+FP+FN+TN}} \tag{13}$$

$$\mathrm{Dice}=\frac{2\times \mathrm{TP}}{\mathrm{FP}+2\times \mathrm{TP+FN}} \tag{14}$$

$$\mathrm{IoU}=\frac{\mathrm{TP}}{\mathrm{FP+TP+FN}} \tag{15}$$

$$\mathrm{MIoU}=\frac{|A\cap B|}{|A|+|B|-|A\cap B|} \tag{16}$$

Among them, TP represents the number of correctly predicted positive samples, and FP represents the number of samples that are actually negative but incorrectly predicted as positive. FN represents the number of samples that are actually positive but incorrectly predicted as negative. A represents the predicted result, B represents the true label.

ISSN 2616-5775 Vol. 9, Issue 5: 9-19, DOI: 10.25236/AJCIS.2026.090502

4. Experimental results and analysis

4.1 Performance Evaluation of SHDSY-Net on PT Dataset

The aim of this study is to evaluate the contribution of each module to the task of detecting and segmenting pregnancy tissue through ablation experiments. According to Table 2, YOLOv8 serves as the benchmark backbone network to form the experimental baseline, and YOLOv8+H integrates the HSFPN module into the YOLOv8 backbone network. YOLOv8+H+D integrates DWR Seg extended residual module on this basis. YOLOv8+H+D+S further integrates SA Head lightweight self-attention detection head module. In addition, to verify the effectiveness of transfer learning, this paper uses a semi supervised learning method to train the SHDSY Net network, combining a small amount of finely labeled data with a large amount of unlabeled data. And using pre trained weights on the ACDC dataset for transfer learning of SHDSY Net, followed by fine-tuning on the PT dataset, the final accuracy reached 92.31%, recall rate reached 92.03%, F1 score reached 91.61%, accuracy reached 93.84%, and Dice coefficient reached 92.63%. All models are trained for 200 rounds, with input sizes adjusted to 640 × 640, and various types of samples are balanced to evaluate the detection and segmentation performance of different types of targets. Figure 5 shows the visualization results of segmentation of pregnant tissue. Among them, the red area represents the segmentation mask of the decidual tissue DT, and the pink area represents the segmentation mask of the gestational sac GS.

Table 2: Experimental results of gestational sac and decidual tissue

Method	*P*(%)		*R*(%)		F1(%)		*AP*(%)	
	GS	*DT*	*GS*	*DT*	*GS*	*DT*	*GS*	*DT*
YOLOv8	80.95	81.63	79.07	82.46	79.99	82.02	84.33	82.92
YOLOv8+H	82.92	82.61	80.95	80.85	81.92	81.72	85.57	83.33
YOLOv8+H+D	83.95	84.78	85.01	82.98	84.47	84.05	87.56	85.07
YOLOv8+H+D+S	86.23	85.51	86.84	84.78	86.54	85.24	89.06	86.94
SHDSY-Net	**89.18**	**90.96**	**90.47**	**88.89**	**90.31**	**89.92**	**90.43**	**88.31**

Continued Table 2

Method	*Dice*(%)		*IoU*		AP_{50}^{val}(%)	
	GS	*DT*	*GS*	*DT*	*GS*	*DT*
YOLOv8	80.00	82.05	69.67	69.57	78.56	79.88
YOLOv8+H	81.93	81.72	69.39	69.09	81.10	80.35
YOLOv8+H+D	84.47	83.87	73.12	72.23	83.80	82.60
YOLOv8+H+D+S	86.27	85.25	75.86	74.29	86.20	84.50
SHDSY-Net	**89.31**	**90.91**	**83.07**	**85.43**	**93.20**	**92.40**

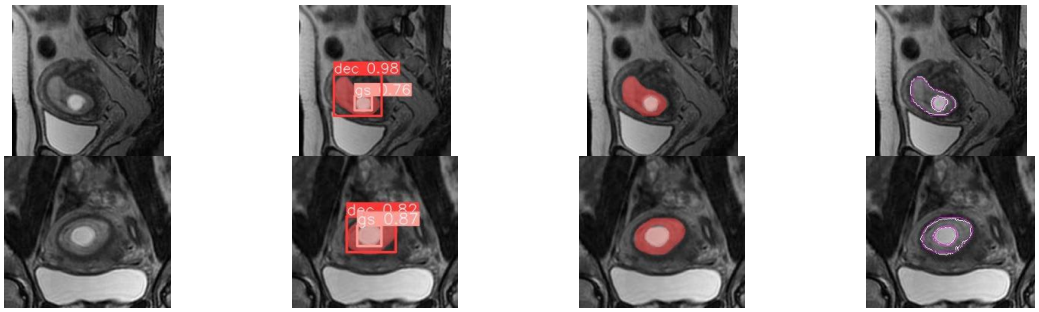

(*a*) (*b*) (*c*) (*d*)

Figure 5: Visualization results of the model for detection and segmentation of the pregnancy tissue. (a) is the original image, (b) is the visualized detection result, (c) is the visualized segmentation result, (d) is the comparison of the contours of the area representing the pregnancy tissue.

4.2 CSP Testing Experiment Results and Analysis

Owing to the firm adherence of gestational tissue to the uterine wall, implantation within the scar region of the anterior lower uterine segment carries a substantially elevated risk of severe hemorrhage. This study utilizes the SHDSY Net for the detection of severe bleeding in patients with cesarean scar

ISSN 2616-5775 Vol. 9, Issue 5: 9-19, DOI: 10.25236/AJCIS.2026.090502

pregnancy (CSP).

The detection results of SHDSY Net model in CSP hemorrhage are shown in Figure 6, which displays the visualization results of four samples. The light blue area in the figure represents the detection area where CSP does not bleed heavily, and the dark blue target box represents the detection area where CSP bleeds heavily. Table 3 shows the logistic regression analysis of predicting the risk of major bleeding in MRI.

Table 3: Logistic regression analysis of predicting the risk of major bleeding in MRI

MRI test results	Non-major bleeding	Major bleeding
Thickness of uterine scar(mm)	3.08[2.56-3.61]	1.09[0.65-1.53]
Depth of Cesarean Diverticulum (mm)	5.26[4.47-6.05]	10.17[9.48-10.86]
Area of cesarean section diverticulum(mm^2)	80.73[59.07-102.39]	316.85[244.45-389.26]

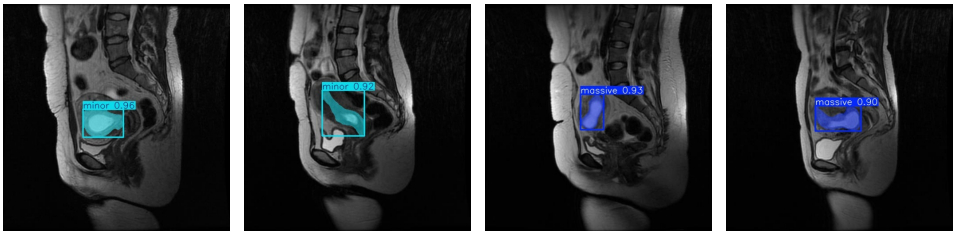

Figure 6: Visualization results of 4-samples

4.3 Performance Evaluation of SHDSY-Net on ACDC Dataset

SHDSY Net was compared with other semi supervised methods on the ACDC dataset. Table 4 shows the quantitative results of detection and segmentation for the ACDC dataset.

Table 4: The detection and segmentation performance of SHDSY-Net on the ACDC dataset

Method	P(%)				R(%)				F1(%)			
	RV	MY	LV	Overall	RV	MY	LV	Overall	RV	MY	LV	Overall
YOLOv8	80.71	81.36	81.25	81.11	79.31	80.75	82.53	80.86	79.99	81.05	81.88	80.97
YOLOv8+H	82.61	84.21	82.75	83.19	80.85	82.76	85.71	83.11	81.74	83.48	84.21	83.14
YOLOv8+H+D	84.23	86.71	86.21	85.72	82.35	83.69	87.75	84.59	83.28	85.17	86.97	85.14
YOLOv8+H+D+S	87.51	88.89	89.66	88.69	85.71	86.27	88.14	87.71	86.59	87.56	88.92	88.69
SHDSY-Net(Ours)	**90.47**	**92.31**	**92.85**	**91.88**	**88.37**	**88.89**	**91.23**	**89.51**	**89.41**	**90.56**	**92.03**	**90.67**

Continued Table 4

Method	AP(%)				Dice(%)				AP50(%)			
	RV	MY	LV	Overall	RV	MY	LV	Overall	RV	MY	LV	Overall
YOLOv8	80.71	81.36	81.25	81.11	79.31	80.75	82.53	80.86	79.99	81.05	81.88	80.97
YOLOv8+H	82.61	84.21	82.75	83.19	80.85	82.76	85.71	83.11	81.74	83.48	84.21	83.14
YOLOv8+H+D	84.23	86.71	86.21	85.72	82.35	83.69	87.75	84.59	83.28	85.17	86.97	85.14
YOLOv8+H+D+S	87.51	88.89	89.66	88.69	85.71	86.27	88.14	87.71	86.59	87.56	88.92	88.69
SHDSY-Net(Ours)	**90.47**	**92.31**	**92.85**	**91.88**	**88.37**	**88.89**	**91.23**	**89.51**	**89.41**	**90.56**	**92.03**	**90.67**

From Table 4, it can be seen that the accuracy of SHDSY Net has increased by 10.77%, recall rate has increased by 8.86%, F1 score has increased by 9.70%, accuracy has increased by 9.70%, similarity coefficient Dice has increased by 9.02%, average intersection to union ratio has increased by 9.65%, and MAP50 has increased by 10.20% compared to YOLOv8 network.

5. Discussion and Conclusion

This study proposes a semi-supervised learning model that not only improves the accuracy of feature extraction, but also enhances the model's capacity to integrate multi-scale contextual information. Previous research has primarily focused on the detection and segmentation of gestational tissue, typically employing various network architectures. Gestational tissue exhibits significant morphological variations and substantial inter-individual differences during early pregnancy, which increases the difficulty of detection and segmentation. Both fully supervised and semi-supervised variants of the proposed network were validated and evaluated on the PT dataset and the ACDC dataset.

ISSN 2616-5775 Vol. 9, Issue 5: 9-19, DOI: 10.25236/AJCIS.2026.090502

The experimental results demonstrate that, on the PT datasets, the semi-supervised segmentation model achieved a Dice coefficient of 90.48%. For semi-supervised detection, the accuracy, recall, and F1 score reached 89.88%, 90.17%, and 89.96%, respectively, outperforming comparable models. The proposed model achieved a Dice coefficient of 90.34% for semi-supervised segmentation of the left ventricle, myocardium, and right ventricle, with detection accuracy, recall, and F1 score of 91.88%, 89.51%, and 90.67%, respectively, surpassing those of other semi-supervised models. Although the proposed model performed well under experimental conditions, several challenges remain in its clinical application. Future work will focus on validating the model across multiple datasets, evaluating its applicability in diverse clinical scenarios, and integrating it into clinical workflows. We will further optimize the model architecture, improve its performance on complex clinical data, and explore its potential applications in other medical image segmentation tasks. Additional gynecological diseases will be incorporated into the dataset to enable the detection and segmentation of multiple conditions, thereby enhancing the generalizability and robustness of the proposed model.

References

[1] Timor-Tritsch I E, Horwitz G, D'Antonio F, et al. Recurrent cesarean scar pregnancy: case series and literature review[J]. Ultrasound in Obstetrics & Gynecology: The Official Journal of the International Society of Ultrasound in Obstetrics and Gynecology, 2021,58(1):121-126.

[2] Al-Jaroudi D, Aboudi S, Baradwan S. Different treatment modalities for cesarean scar pregnancies: a single-center experience and literature review[J]. Archives of Gynecology and Obstetrics, 2021, 303(5):1143-1151.

[3] Laure N, Basky T. Caesarean scar pregnancy: diagnosis, natural history and treatment[J]. Current Opinion in Obstetrics & Gynecology,2022,34(5):279-286.

[4] Lucrezia V D B, Jure K, Dimitrios M, et al. Risk prediction of major haemorrhage with surgical treatment of live cesarean scar pregnancies[J]. European Journal of Obstetrics, Gynecology and Reproductive Biology: An International Journal,2021,264:224-231.

[5] Hua A, Igel C, Fridman D, et al. Direct visualization of a cesarean scar ectopic pregnancy after medical management[J]. American Journal of Case Reports, 2024,25: e944396.

[6] Kavita K, Deepika S, Ramya M, et al. Laparoscopic excision of cesarean scar ectopic pregnancy: an optimum management option[J]. Gynecology and Minimally Invasive Therapy,2024,13(2):119-122.

[7] Lei Yan, Zhang Na, Liu Yu, et al. A prediction nomogram for residual after negative pressure aspiration for endogenic cesarean scar ectopic pregnancy: a retrospective study[J]. BMC Pregnancy and Childbirth, 2025,25(1):1-13.

[8] Lei Yongfeng, Yang Mei, Du Jianxun, et al. Application of three-dimensional ultrasound and MRI in early diagnosis of cesarean scar pregnancy[J]. Chinese Journal of CT and MRI, 2022(7):140-142.

[9] Yu Xianbo, Li Dan, Li Chengcheng, et al. The value of 3.0T MRI combined with transvaginal ultrasound in the diagnosis of cesarean scar pregnancy [J]. Health Guide, 2021(48): 139-141.

[10] Kennedy A, Debbink M, Griffith A, et al. Cesarean scar ectopic pregnancy: a Do-Not-Miss diagnosis[J]. Radiographics,2024,44(7): e230199.

[11] Shahedi M, Dormer J D, Herrera C, et al. Deep learning-based segmentation of the placenta and uterus on MR images[J]. Journal of Medical Imaging,2021,8(5):054001.

[12] Guo Lei, Li Liming, Lin Chulan, et al. Application of an improved Swin-Unet with wavelet convolution and attention mechanism for MRI segmentation in HIFU treatment of uterine fibroids[J]. Guangdong Medical Journal, 2025, 46 (11): 1606-1613.

[13] Singh T G, Karthik B, Wahengbam M. An ensemble approach for uterine pathology classification in MRI imaging using deep learning[C]//International Conference on Sustainable Communication Networks and Application,2023:1672-1677.

[14] Cai Peiya, Yang Tiantian, Xie Qinglai, et al. A lightweight hybrid model for the automatic recognition of uterine fibroid ultrasound images based on deep learning[J]. Journal of Clinical Ultrasound: JCU,2024,52(6):753-762.

[15] Yin Chenghuan, Wang Yu, Zhang Qixin, et al. An accurate segmentation framework for static ultrasound images of the gestational sac[J]. Journal of Medical and Biological Engineering, 2022,42(1):49-62.

[16] Zong Ming, Pei Xinlong, Luo Yangyu et al. Deep learning model based on multisequence MRI images for assessing adverse pregnancy outcome in placenta accreta[J]. Journal of Magnetic Resonance Imaging: JMRI, 2024, 59(2):510-521.

[17] El-Khatib M, Teodor O, Popescu D, et al. Using combined CNNs for ROI segmentation in early investigation of pregnancy[C]//IEEE International Conference on Control, Decision and Information Technologies, 2022: 897-902.

ISSN 2616-5775 Vol. 9, Issue 5: 9-19, DOI: 10.25236/AJCIS.2026.090502

[18] Li Qian, Dai Chengcheng, Zhang Junhui, et al. Construction of a nomogram model for predicting massive hemorrhage during hysteroscopic cureage in cesarean scar pregnancy and risk stratification based on multimodal ultrasound parameters[J]. Clinical Misdiagnosis & Mistherapy, 2025, 38 (14): 45-50.

[19] Zhang Shujun, Peng Zhong, Li Hui. SAU-Net: A Medical Image Segmentation Method Based on U-Net and Self-attention Mechanism [J]. Chinese Journal of Electronics, 2022, 50 (10): 2433-2442.

[20] Yan Zijie, Wang Yang, Chen Yan, et al. Semi-supervised rock slice image classification based on hierarchy consistency mean teacher model[J]. Journal of Applied Sciences, 2024, 42 (1): 27-38.

[21] Shi Dianxi, Liu Yangyang, Song Linna, et al. FeaEM: feature enhancement-based method for weakly supervised salient object detection via multiple pseudo labels[J]. Computer Science, 2024, 51 (1): 233-242.

[22] Xu Siyi, Wang Jian, Sang Qingbing. Semi-supervised method for underwater object detection algorithm based on improved YOLOv8[J]. Applied Sciences,2025,15(3): 2076-3417.

[23] Li Fei, Liu Zepeng, Wang Yizong, et al. Brain tumor medical image algorithm detection based on YOLOv9 algorithm[J]. Digital Technology and Applications, 2025, 43 (1): 195-198.

[24] Chen Yifei, Zhang Chenyan, Chen Ben, et al. Accurate leukocyte detection based on deformable-DETR and multi-level feature fusion for aiding diagnosis of blood diseases[J]. Computers in Biology and Medicine, 2024,170:0010-4825.

[25] Ye Yuxin, Ju Zhiyong, Lai Ying. Traffic sign detection algorithm incorporating receptive field enhancement module and attention mechanism[J]. Electronic Science and Technology, 2024, 37 (6): 8-16.

[26] Yang F, Yang X, Jing H, et al. MRI-based scoring model to predict massive hemorrhage during dilatation and curettage in patients with cesarean scar pregnancy[J]. Abdominal Radiology. 2023 Oct;48(10):3195-3206.